Boundary-Layer Meteorology (2021) 181:473–498
https://doi.org/10.1007/s10546-020-00599-6

RESEARCH ARTICLE

Investigating the Sensitivity of Marine Fog to Physical and Microphysical Processes Using Large-Eddy Simulation

Charlotte Wainwright[1] · **David Richter**[1]

Received: 15 May 2020 / Accepted: 19 December 2020 / Published online: 17 January 2021

Abstract
Over the past few years large-eddy simulation (LES) has demonstrated success in modelling continental radiation fog, and several recent studies have used LES to investigate the sensitivity of fog formation to physical processes such as turbulent mixing and surface heat and moisture exchange, as well as to the parametrization of microphysical processes such as cloud droplet activation. Here we extend these sensitivity studies to marine fog. There are several important differences in the formation of marine and continental fog, however moisture availability is no longer a decisive factor, and surface temperature changes over a much longer time scale. Here LES is used to examine the sensitivity of simulated marine-fog formation and maintenance to the cloud-droplet number concentration, turbulent mixing, and air–sea temperature difference. The strength of the fog (in terms of liquid water content) is found to be highly sensitive to all three factors. Varying only the cloud-droplet number concentration, even within a range of physically realistic values for marine regions, can mean the difference between fog halving or doubling in liquid water content. The sensitivities demonstrated herein indicate the great need and challenge for constraining these parameters in numerical weather prediction. Similarities and differences to the findings for continental radiation fog are examined, and important considerations for future improvements in marine-fog forecasting are discussed.

Keywords Fog · Large-eddy simulation · Marine fog · Sensitivity study

1 Introduction

Marine fog can have a significant impact on human activities in coastal and ocean areas. Considerable economic costs result from the disruption to transportation by sea, land, and air, with financial losses from fog as high as those due to severe convective storms or in some cases even winter weather (Gultepe et al. 2007). In fog-prone regions such as the Grand Banks region of the north Atlantic (Dorman et al. 2017), the occurrence of marine fog introduces considerable logistical challenges to offshore industries such as oil platforms that rely on regular availability of air or sea transport (e.g., Isaac et al. 2020). In nearby coastal areas, fog

✉ Charlotte Wainwright
cwainwri@nd.edu

[1] University of Notre Dame, 156 Fitzpatrick Hall, Notre Dame, IN 46556, USA

occurrence can be extremely frequent during certain times of the year, significantly affecting road transportation and safety. The Fog Remote Sensing and Modelling Campaign (FRAM, Gultepe et al. 2009) found fog occurrence over 50% of the time on the Nova Scotia coastline during the summer months.

Despite considerable progress in operational numerical weather prediction (NWP) modelling, however, improvements to fog forecasts have lagged behind other areas, and accurate forecasting of the onset time, thickness, and duration of fog remains challenging (van der Velde et al. 2010). This is due to the complex interplay of physical and microphysical processes that govern fog formation, maintenance, and dissipation, and the wide range of time and spatial scales upon which these processes operate (Porson et al. 2011; Dorman and Koračin 2017).

The advent of large-eddy simulation (LES) has spurred a new generation of numerical studies of fog formation, beginning with Nakanishi (2000). Since the early 2000s this area has attracted greater interest, yet there remain inherent difficulties in accurately representing the stable boundary layer (SBL) in LES (see Beare et al. 2006). The development of fog in both mesoscale and high-resolution simulations (i.e., LES) is known to be sensitive to many physical processes that are typically represented using coarse parametrization schemes, including land–atmosphere exchange, radiation, microphysics, as well as complex interactions between the schemes (e.g., Duynkerke 1999; Gultepe et al. 2007; Haeffelin et al. 2010; Maronga and Bosveld 2017).

One of the difficulties in modelling fog using LES is that fine grid spacing is required in order to adequately capture the necessary processes important for fog formation in sufficient detail (Tardif 2007; van der Velde et al. 2010; Kim and Yum 2012a). Several previous LES studies have used grid spacings below 5 m to investigate radiation fog (e.g., Nakanishi 2000; Porson et al. 2011; Bergot 2013; Poku et al. 2019), and the sensitivity of fog to grid spacing was investigated by Maronga and Bosveld (2017, hereafter MB17), who systematically tested grid spacings between 0.5 and 4 m. Their study found that, although the 4-m grid spacing reproduced key features of the fog life cycle, the fog-formation time was highly sensitive to grid spacing. Based on their tests, a grid spacing of 1 m was chosen for the remainder of their study and for follow-up work (Schwenkel and Maronga 2019) to balance the need of adequately resolving the small near-surface turbulent eddies with the large computational expense required by such fine grid spacing.

Correct handling of the surface exchange is of vital importance for the formation of fog. For land-based fog, Duynkerke (1991) showed using a one-dimensional model that vegetation must be represented appropriately in order to reproduce the correct soil moisture and temperature. This is particularly relevant for continental fog where moisture availability or the lack thereof may be a deciding factor in whether fog develops or not. Accurate parametrization of the air–sea interaction is also necessary for modelling marine fog, even though the temporal and spatial scales over which the sea-surface temperature (SST) changes are larger than the corresponding scales over land. For instance, Fallmann et al. (2019) demonstrated that the inclusion of dynamic coupling of the atmosphere and ocean in the UKC3 regional mesoscale model resulted in improvements to modelled fog extent and visibility compared to an uncoupled atmosphere-only simulation.

The vast majority of LES studies on fog in the literature have focused on continental radiation fog (e.g., Nakanishi 2000; Porson et al. 2011; Bergot 2013, 2016; MB17). The radiative transfer parametrization scheme is clearly of utmost importance for these types of simulations, in which radiative cooling is a controlling factor. The interaction of the radiation scheme with both the surface exchange and microphysical processes is also of significant interest. It was shown by Edwards (2009) that accurate representation of radiative cooling,

along with high vertical grid spacing in the surface layer, is required to produce accurate radiative flux divergence in the lowest few metres of the atmosphere. Once fog is optically thick, radiative cooling at the fog top also becomes increasingly important (Brown and Roach 1976; Duynkerke 1999) and so interactions between the radiative and microphysical parametrization schemes also play a role.

Fog formation is also sensitive to several aspects of the microphysical scheme. This includes whether the cloud-droplet number concentration (N_c) is held fixed or if cloud droplets are activated based upon supersaturation (following Twomey (1959) and extensions thereof) or a background aerosol content (e.g., Abdul-Razzak and Ghan 2000). If N_c is fixed then the value selected can significantly alter the fog liquid water content (MB17); if cloud droplets are activated from a given aerosol distribution then the aerosol concentration strongly affects the fog life cycle (Stolaki et al. 2015; Maalick et al. 2016). The handling of supersaturation has also been shown to have significant impacts on the development of fog in numerical simulations. Observations in both continental radiation fog (e.g., Hammer et al. 2014) and marine fog (Hudson 1980) have shown that supersaturation can persist at levels of approximately 0.1%, yet in numerical simulations all supersaturation is typically removed within a model timestep via condensation and droplet activation. However, Thouron et al. (2012) called into question whether the saturation adjustment scheme is appropriate for use in LES of the SBL since the timesteps involved in the saturation adjustment scheme are often longer than the timesteps required for LES of stable conditions. Boutle et al. (2018) and Schwenkel and Maronga (2019) recently performed LES of radiation fog using microphysics schemes that explicitly calculate supersaturation, and therefore do not automatically eliminate it at each timestep. Both sets of authors found that allowing supersaturation to persist reduced the fog liquid water content by slowing the transition to optically thick fog and the consequent positive feedback between condensation and radiative cooling. The immediate removal of supersaturation may be of particular importance in modelling of marine fog; it is suggested that higher effective supersaturations occur in marine fog due to the decreased number of cloud condensation nuclei in marine environments as compared to more anthropogenically influenced continental environments where supersaturation can be suppressed by competition between numerous droplets in more highly polluted air (Koračin et al. 2014). The treatment of cloud droplet settling within the microphysics scheme also has a strong impact on fog evolution (Brown and Roach 1976; Nakanishi 2000).

The role of turbulent mixing in fog is multifaceted and has long been a point of discussion. Once fog has developed, turbulent mixing within the fog layer can lead to further growth and deepening, but increased turbulent mixing at the fog top can also lead to the entrainment of dry air which speeds up dissipation. Measurements of turbulence in continental radiation fog suggest that there may exist a threshold value above which turbulence levels preclude fog development (Price et al. 2018), although observations from the upper levels of coastal fog indicate that higher levels of turbulence can persist there (Li and Zheng 2015). The impact of turbulent mixing on the life cycle of radiation fog is investigated numerically by MB17, who find that increased turbulent mixing in general results in the fog becoming stronger and deeper (hereafter "fog strength" is defined in terms of the liquid water content). They also show that either strong increases or decreases in the turbulent mixing via changes in the geostrophic wind speed lead to delays in fog formation, highlighting the complex relationship between fog and turbulent mixing. As turbulence plays a substantial role in whether or not fog will form, very fine grid spacing is required for LES of the SBL in order to resolve as much of the turbulence as possible, though the subgrid model is still an important consideration. Previous LES of radiation fog has been performed using both a Smagorinsky (1963) subgrid turbulence scheme (e.g., Nakanishi 2000; Porson et al. 2011) and one based on Deardorff (1980) (e.g.,

Bergot 2013; MB17; Wærsted et al. 2019). It was found by Porson et al. (2011) that when the Smagorinsky subgrid scheme is used the results of fog simulations were sensitive to the choice of the effective Smagorinsky constant C_s.

In this paper, recent work from MB17 that investigates the sensitivity of continental radiation fog to physical and microphysical processes is extended to the marine environment. We perform a set of idealized large-eddy simulations of marine fog. Our aim is to test the sensitivity of the fog thickness and life cycle to the cloud-droplet number concentration, turbulence, radiation, and air–sea temperature difference, and describe processes that result in these sensitivities. It should be noted that, although the model set-up and initial profile were selected to closely resemble environmental conditions observed during the C-FOG observational campaign, the simulation results are not compared directly back to shipboard observations from a specific case study. Although the shipboard observations include a number of interesting marine fog cases (see Fernando et al. 2020; Wang et al. 2020; Wagh et al. 2020), the complex nature and large-scale effects present in these cases preclude direct, meaningful comparisons. In Sect. 2 the LES code and selected parametrizations are described and details are provided of the simulations performed. Section 3 presents the results of the simulations and provides comparisons to previous findings, while Sect. 4 summarizes the study and discusses remaining challenges and future research directions.

2 Model Set-up

To investigate the impact of different physical and microphysical processes on the formation and maintenance of marine cold advection fog, Cloud Model 1 (CM1, Bryan and Morrison 2011, version 19.6) is used in its LES configuration. Idealized initial baseline simulations are performed at 1-m horizontal grid spacing with $nx = ny = 256$. The vertical grid is stretched with grid spacing of 0.1 m close to the surface and 1.9 m at the model top at 128 m. There are 21 vertical levels within the lowest 5 m and 128 levels below 128 m. Additional levels at higher altitudes were included to ensure correct coupling with the radiation scheme, however these are not dynamically relevant for the domain of interest and are not discussed further. Doubly periodic boundary conditions were used in the lateral directions, and the flow is forced with a constant pressure gradient applied via a specified geostrophic wind speed U_g in the x direction. The simulation is run for 12 hours.

Cloud Model 1 uses a simplified lower surface scheme with a fixed surface enthalpy exchange coefficient of 1.2×10^{-3} based on Drennan et al. (2007). The surface exchange coefficient for momentum is based on Fairall et al. (2003) at low wind speeds and Donelan et al. (2004) at high wind speeds. The subgrid turbulence scheme is based on Deardorff (1980).

As described above, the simulations are performed with a horizontal grid spacing of 1 m. Tests are also performed with horizontal grid spacings of 4 m, 2 m, and 0.5 m, as in MB17, and the results confirm that, for a grid spacing of 1 m, approximately 90% of the turbulence kinetic energy (TKE, e) within the fog layer is resolved (not shown). When the grid spacing was increased to 2 m, 80–85% of the turbulence is resolved, while at 4 m grid spacing less than 70% of e is resolved. Conversely, when the grid spacing is reduced to 0.5 m there is no clear improvement in terms of the fraction of resolved TKE compared to the grid spacing of 1 m. Therefore, as reducing the grid spacing beyond 1 m does not provide significant improvements in resolved TKE, 1-m horizontal grid spacing is used for all simulations. Due to the stretched vertical grid which provides very high vertical resolution in the surface layer,

additional tests of vertical grid spacing are not conducted. Most previous LES studies of fog have used isotropic grid spacing, but we use finer grid spacing in the vertical direction close to the surface in order to resolve more of the turbulence close to the air–sea interface. Additional tests were conducted using an isotropic grid spacing of 2 m, and there was little change in the fog strength and timing (not shown), but the percentage of resolved e was much lower.

2.1 Radiation Scheme

Correct modelling of longwave and shortwave radiative forcing has been demonstrated to be crucial for realistic fog development. Herein the Rapid Radiative Transfer Model (RRTMG, Iacono et al. 2008; designed for global models) is used. The RRTMG scheme operates as a single-column model on each vertical column of the LES independently, which for the statistically homogeneous conditions in the horizontal directions would provide nearly the same result as the radiation model acting on the horizontal mean profile (i.e., the LES domain representing the grid cell of a mesoscale model). Profiles of temperature, pressure, and mixing ratio are passed from the LES code to the radiation scheme, and latitudinally and longitudinally-dependent standard atmospheric profiles are used to extend these data to the top of the atmosphere. The upward, downward, and net longwave and shortwave fluxes are calculated and passed back to the LES code before being used in the temperature and energy budgets. For the simulations herein the latitude and longitude are set as 47.5°N and 52.25°W, and the date and time as 1200 UTC (local time = UTC–2.5 h) on 15 October 2018. This location represents the coastal region east of Newfoundland, Canada, which was the subject of the recent C-FOG experimental campaign that took place during autumn 2018 (Fernando et al. 2020). Sunset on this date occurs at 2039 UTC (1809 local time), approximately 8.5 h into the simulation. The radiation scheme is called at 5-min intervals to reduce computational cost.

2.2 Microphysics Scheme

The Morrison microphysics scheme (Morrison et al. 2005) is used for all of the simulations herein. In this scheme each hydrometeor class is represented using a gamma droplet size distribution of the form

$$f(D) = N_0 D^{p_c} \exp(-\lambda D), \tag{1}$$

in which D is the droplet diameter, N_0 is the intercept parameter, λ is the slope parameter, and p_c is the spectral shape parameter. For cloud droplets p_c is a function of atmospheric pressure and temperature,

$$p_c = \frac{1}{\left(0.0005714\left(\frac{N_c \rho_a}{1\times10^6}\right) + 0.2714\right)^2} - 1, \tag{2}$$

and is constrained between 2 and 10. In Eq. 2, ρ_a is the air density and N_c the cloud-droplet number concentration. The intercept parameter N_0 and slope parameter λ are calculated as

$$N_0 = \frac{N\lambda^{p_c+1}}{\Gamma(p_c+1)}, \tag{3}$$

and

$$\lambda = \left[\frac{cN\Gamma(p_c + d + 1)}{q\Gamma(p_c + 1)}\right]^{1/d}, \tag{4}$$

respectively, where Γ is the Gamma function and $m = cD^d$ is the mass–diameter relationship with c and d constants. The value of λ is constrained in order to keep the mean cloud-droplet particle diameter between 0.1 and 30 μm.

The prognostic equation for mixing ratio of cloud droplets (q_c) in the Morrison microphysics scheme is given by

$$\frac{\partial q_c}{\partial t} = -\nabla \cdot (\mathbf{v} q_c) + \frac{\partial}{\partial z}(V_{q_c}) + \nabla_D q_c + \left(\frac{\partial q_c}{\partial t}\right)_{\text{ACT}} + \left(\frac{\partial q_c}{\partial t}\right)_{\text{COND/DEP}}, \tag{5}$$

while the prognostic equation for cloud-droplet number concentration (N_c) is

$$\frac{\partial N_c}{\partial t} = -\nabla \cdot (\mathbf{v} N_c) + \frac{\partial}{\partial z}(V_{N_c}) + \nabla_D N_c + \left(\frac{\partial N_c}{\partial t}\right)_{\text{ACT}} + \left(\frac{\partial N_c}{\partial t}\right)_{\text{EVAP/SUB}}. \tag{6}$$

The first three terms on the right-hand side of Eqs. 5 and 6 represent advection, sedimentation, and diffusion. The fourth term represents activation of cloud droplets, and the fifth contributions from condensation, evaporation, deposition and sublimation. Additional terms are included for contributions from autoconversion between the cloud droplet and rain classes resulting from coalescence and growth by diffusion, self-collection, collection between hydrometeor species, and melting/freezing, but these are not important for this case and will not be discussed further.

In the Morrison microphysics scheme the cloud-droplet number concentration can either be prognosed via Eq. 6 in a two-moment configuration, or held at a constant user-defined value in a single-moment configuration where the cloud-droplet mixing ratio is the only moment prognosed. For all of the simulations in this study N_c is held constant (i.e., we use a one-moment scheme), to allow us to systematically investigate the effect that changing the value of N_c has on the fog characteristics and life cycle, as in MB17 and Poku et al. (2019).

At the end of each model timestep, a saturation adjustment scheme is applied which immediately removes all water vapour above saturation via condensation and activation of new cloud droplets. When the cloud-droplet number concentration is held fixed, new droplets cannot be activated in grid cells that already contain cloud droplets and so the droplet effective radius (r_{eff}) is instead adjusted accordingly in order to reduce saturation to 100%.

2.3 Initial Profile

A simplified initial profile is used, based on representative conditions encountered during the C-FOG research cruise. The same initial profile is used for each simulation to enable us to isolate the effects of varying the cloud-droplet number concentration, turbulent mixing, and air–sea temperature difference ΔT. In the initial profile the potential temperature increases with height from 284 K at the surface to 284.5 K at 95 m (Fig. 1a), with a relative humidity of 98.9–99.2% through this layer. Between 95 and 120 m, the water vapour mixing ratio decreases from 8.0 to 6.6 g kg^{-1}, and the relative humidity decreases from 99 to 80% across this layer (Fig. 1c). For the baseline simulation the initial value of u is set equal to $U_g = 3$ m s^{-1} throughout the domain and the initial value of $v = 0$. The value of U_g is varied for the sensitivity tests as outlined in Table 1 and the initial value of v is kept at zero for all simulations.

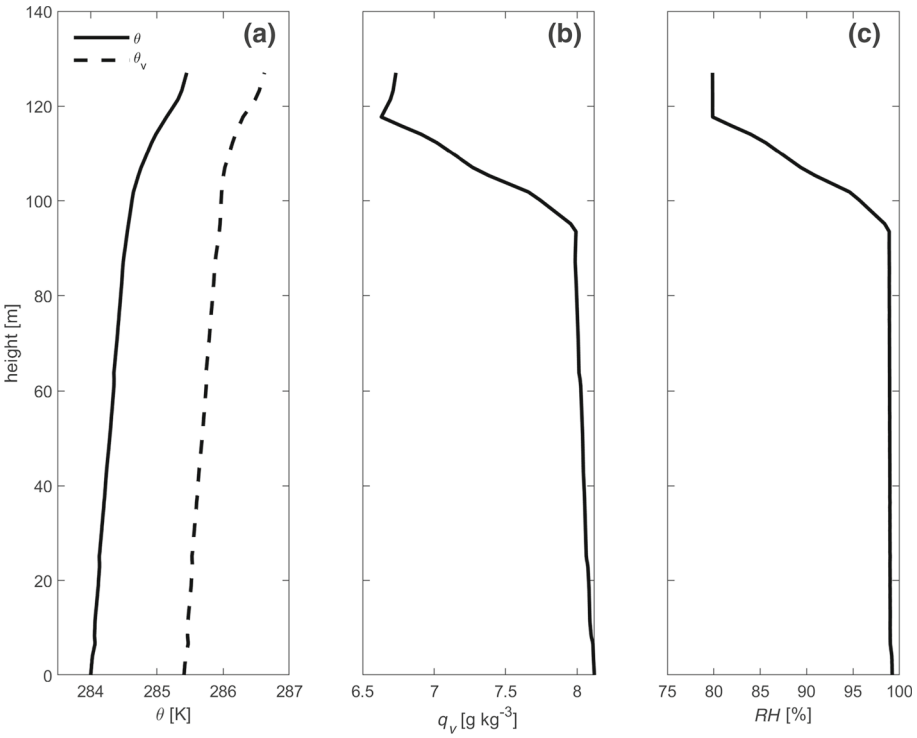

Fig. 1 Initial vertical profiles of **a** potential temperature and virtual potential temperature, **b** water vapour mixing ratio, and **c** relative humidity used for all of the simulations

2.4 Sensitivity Testing

In order to test the sensitivity of the fog thickness and life cycle to various model parameters, several numerical tests are performed. These are described briefly here and listed in Table 1. The baseline simulation (hereafter BASE) is performed using the initial profile as described above and illustrated in Fig. 1, with $U_g = 3\,\mathrm{m\,s^{-1}}$. The initial air–sea temperature difference is 2 K, with the sea surface colder than the overlying air. The cloud-droplet number concentration is set at a fixed value of 100 $\mathrm{cm^{-3}}$. The RRTMG radiation scheme is used with the location and start time described in Sect. 2.1.

To test the importance of radiative cooling on the fog development and maintenance, a simulation is performed in which all parameters were held the same as in case BASE, except the radiation scheme was turned off (case NORAD).

Several previous studies have indicated that both the timing and thickness of the fog can be sensitive to the value of the cloud-droplet number concentration (e.g., Maalick et al. 2016; MB17; Poku et al. 2019). This sensitivity is examined by repeating case BASE using a both a lower and higher fixed value for N_c. The original N_c is set at 100 $\mathrm{cm^{-3}}$, and a reduced value of 50 $\mathrm{cm^{-3}}$ (case NC50) and an increased value of 150 $\mathrm{cm^{-3}}$ (case NC150) are tested.

It is also well known that fog formation is highly sensitive to the surface temperature and moisture availability. In this study, a simplified surface scheme is used in which the SST is held fixed; this is a reasonable assumption over an ocean surface for a time scale of 12 hours. All cases use an initial SST of 284 K for the first hour, to allow for turbulence

Table 1 List of simulations conducted

Simulation	N_c (cm^{-3})	Radiation	SST (K)	ΔT (K) after 1 h	U_g (m s^{-1})
BASE	100	Y	282	2	3
NORAD	100	N	282	2	3
NC50	50	Y	282	2	3
NC150	150	Y	282	2	3
TDIFF1	100	Y	283	1	3
TDIFF4	100	Y	280	4	3
U2	100	Y	282	2	2
U4	100	Y	282	2	4

spin-up prior to fog formation. After one hour, the SST is dropped to a constant value for each simulation as listed in Table 1. This process allows the full LES domain to mimic a parcel of air in thermal equilibrium with the water below being advected over colder water 1 h into the simulation—i.e., providing a means for studying advection fog while resolving the turbulence scales.

In case BASE, the near-surface potential temperature is 284 K and the SST is reduced to 282 K after the hour of turbulence spin-up. This ΔT value of 2 K was selected based on Isaac et al. (2020), who showed that the average air–sea temperature difference in the Grand Banks region was 2 K during the summer months, when the occurrence of sea fog is most frequent. The initial potential temperature profile remains the same throughout all the simulations. A reduced air–sea temperature contrast is tested by setting SST to 283 K ($\Delta T = 1$ K, case TDIFF1). Similarly, a higher air–sea temperature difference is tested using a fixed SST of 280 K ($\Delta T = 4$ K, case TDIFF4).

Finally, we follow the method of MB17 and test the sensitivity to turbulent mixing by changing the prescribed geostrophic wind velocity. Case BASE uses a value of $U_g = 3$ m s^{-1}; an additional case with decreased turbulent mixing is tested using $U_g = 2$ m s^{-1} (case U2). The impact of stronger turbulent mixing is examined using an increased geostrophic wind velocity of 4 m s^{-1} (case U4).

3 Results and Discussion

3.1 Baseline Simulation

A snapshot of the liquid water content (LWC) from the baseline simulation (case BASE) at 2-m height and at the lateral boundaries after 12 h of simulation time is shown in Fig. 2 to illustrate the three-dimensional structure of the mature fog. Although the fog covers the full lateral extent of the domain, stripes of lower LWC are clearly visible in Fig. 2 (lighter blue colour), and correspond to regions of slightly higher temperature (not shown). Figure 3 shows time-height plots of domain-averaged quantities of liquid water mixing ratio, potential temperature, and TKE for case BASE. After the one-hour turbulence spin-up, the SST drops from 284 to 282 K, and fog begins to form. Here the height of the fog top is defined using a threshold value of the liquid water mixing ratio $q_l > 0.01$ g kg^{-1} (marked by the white dashed line in Fig. 3a), following MB17. Since the rain water mixing ratio is several orders of magnitude lower than q_c, and q_l is roughly equal to q_c. The initial fog formation at 1

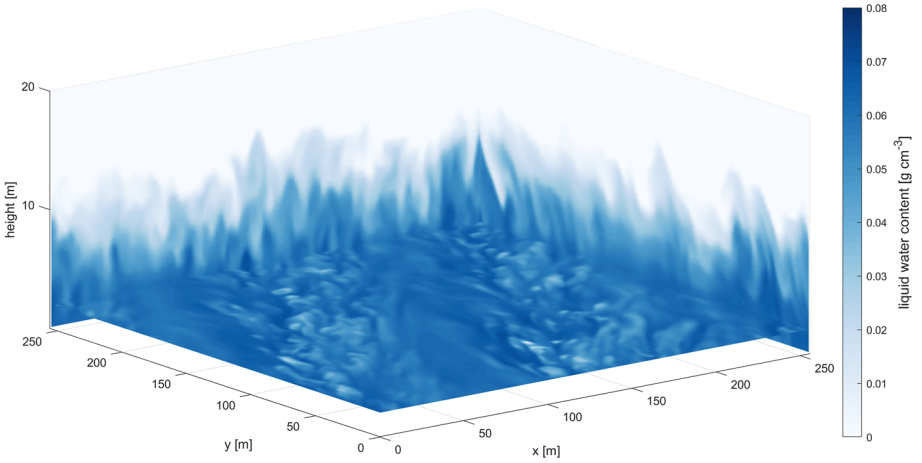

Fig. 2 Instantaneous contours of liquid water content from case BASE at 2-m height and at the lateral boundaries 12 h into the simulation (0000 UTC)

h is caused by the adjustment of the flow to the sudden drop in SST, akin to an air parcel moving over the ocean suddenly encountering a drop in SST due to passage over a current of colder water. The sudden drop in SST creates a strong negative surface θ flux, which decreases in strength as the near-surface air temperature adjusts to the lower SST. The drop in SST causes strongly stable near-surface conditions shortly after 1 h, with $\mathrm{d}\theta/\mathrm{d}z$ in the near-surface region of 0.2 K m^{-1}. As the flow adjusts to the lower SST, the static stability decreases in the near-surface region and the strongest static stability is just above the fog top. As the near-surface air adjusts to the decreased SST, the fog decreases in strength (in terms of q_l) between hours 3 and 5, and remains weaker until 8 h. At 8 h, once the flow has adjusted to the lower SST, the near-surface temperature continues to fall and the fog begins to again increase in strength and depth until the end of the simulation, regardless of the transition from day to night. At this time, θ within the fog layer has fallen below the SST (see Fig. 3b). The height of the maximum q_l remains at the lowest model level until 11 h into the simulation, and within the lowest 1 m throughout. During the final hour of the simulation, the static stability is below 0.05 K m^{-1} in the lowest 5 m, and is highest (above 0.2 K m^{-1}) just above the fog top. The fog shows no signs of dissipating or decreasing in strength towards the end of the simulation. Unlike for continental radiation fog, the ocean surface provides a continual source of moisture, therefore moisture availability never becomes a limiting factor.

Figure 3b shows the planar-averaged potential temperature over the course of the simulation. During the first hour of the simulation, when the SST is 284 K, the surface θ remains almost constant, with a minimal increase due to the incoming solar radiation. Once the SST drops at 1 h, θ at the lowest model level (θ_1) begins to fall, dropping by 1 K within 30 min. The θ_1 value continues to fall until 3.5 h, after which it oscillates between 282.1 and 282.3 K for several hours. This oscillation in θ_1 corresponds to the time period when the fog is weaker, seen in Fig. 3a. After 8 h, θ_1 continues to fall, reaching 282 K (equal to the SST) shortly before 10 h, as indicated by the black dashed line in Fig. 3b. After 12 h, θ_1 is 281.8 K, 0.2 K lower than the SST. Therefore, for most of the simulation the sea surface remains colder than the overlaying air in the fog layer. The impact of changing the SST on the fog development is addressed in Sect. 3.4.

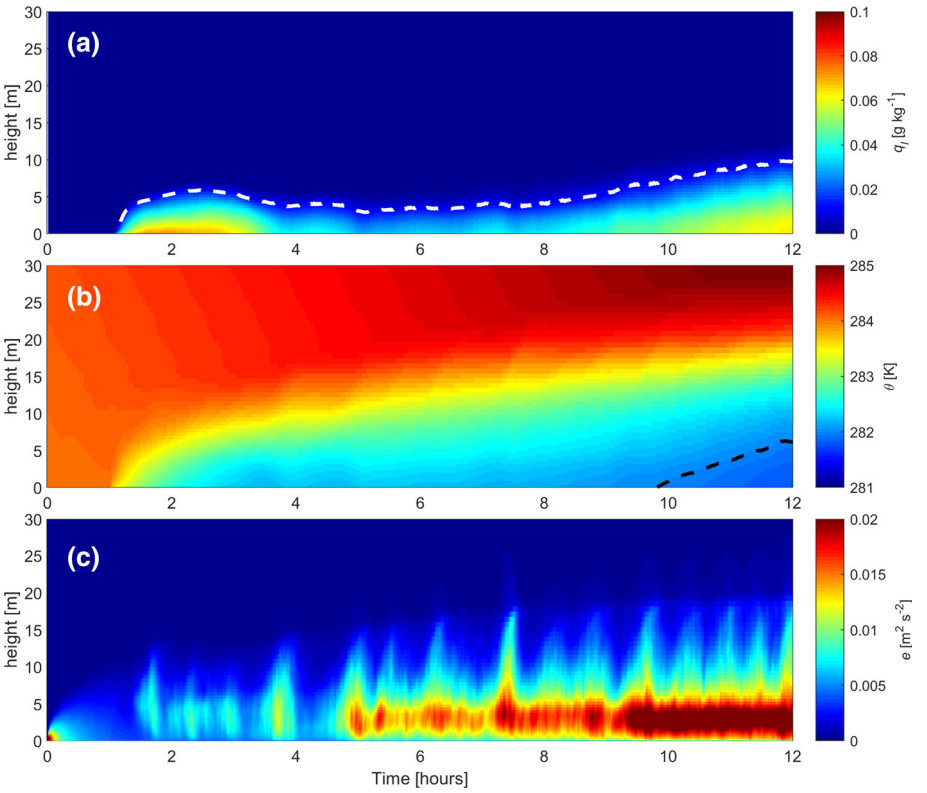

Fig. 3 Time–height plot of domain-averaged variables for case BASE **a** q_l in g kg^{-1}, with the white dashed line showing a contour at $q_l = 0.01$ g kg^{-1}, **b** θ in K with a black dashed line at the height where θ is equal to the constant SST of 282 K, **c** e in m^2 s^{-2}. The simulations are initialized at 1200 UTC

The TKE is shown in Fig. 3c. The highest values of TKE are found within the fog layer, and total TKE is between 0.01 and 0.025 m^2 s^{-2} through the depth of the fog layer. The maximum TKE within the fog layer increases further during the last 2.5 h of the simulation, as the fog continues to grow in strength and depth. At the horizontal resolution of 1 m, we find that at heights over 1 m above the ocean surface, 90% of TKE is resolved (not shown).

3.2 Sensitivity to Radiative Cooling

To test the sensitivity of the fog formation to radiative cooling and to demonstrate that it is a first-order influence on fog development, a simulation is performed that is identical to BASE in all regards except the radiation scheme is turned off (case NORAD). In case BASE, where the RRTMG radiation scheme is used, the maximum horizontally-averaged q_l over the course of the simulation is 0.07 g kg^{-1}. In case NORAD, this is significantly reduced to 0.03 g kg^{-1} (Fig. 4b). Oscillations in the maximum horizontally averaged q_l for case NORAD are also visible in Fig. 4b after 4 h at periods of approximately 60 min, with times of decreased maximum q_l corresponding to increased mixing as evidenced by higher values of TKE (not shown). The time-height plot of q_l for case NORAD shown in Fig. 4a indicates that the vertical extent of the fog is also much smaller, with the fog top remaining below 3

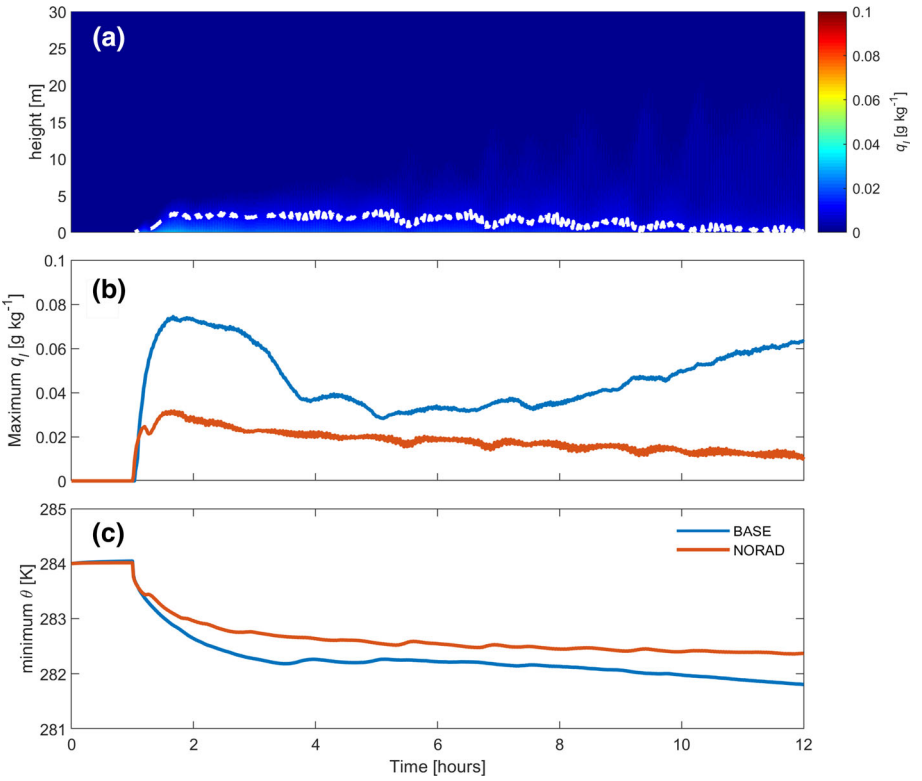

Fig. 4 **a** Time–height plot of domain-averaged q_l for case NORAD, **b** the profile-maximum q_l for cases NORAD and BASE, **c** the minimum domain-averaged θ for cases NORAD and BASE

m throughout the simulation, and generally decreasing in height from 6 h onward. When the radiation scheme is turned off, the lack of radiatively driven cooling also prevents θ from dropping as low as in case BASE (Fig. 4c).

While it is expected that turning off the radiation scheme will reduce the fog strength, the role that longwave radiative cooling plays in fog formation in the baseline simulation is explored in more detail in Fig 5. When the fog initially starts developing from 1 h onward, the radiative cooling rate within the fog layer is between -3 and -4 K h^{-1}, with higher radiative cooling rates close to the surface where q_c is highest. The radiative cooling rate decreases somewhat as the fog strength decreases between 4 and 6 h, and then steadily increases as the fog continues to restrengthen from 8 h onward. After 12 h of simulation, the radiative cooling rate close to the sea surface is -1.8 K h^{-1}. Throughout the simulation, radiative cooling is the strongest cooling mechanism within the bulk of the fog layer, which explains why the fog vertical development is significantly curtailed when the radiation scheme is turned off. For this set-up it is clear that radiative cooling is a critical process in the fog development, and in additional tests conducted using a simplified initial profile with a slightly lower relative humidity throughout the moist layer, when the radiation scheme was turned off θ did not decrease sufficiently for the parcel to reach saturation and so no fog formed (not shown).

Previous LES studies have found radiative cooling rates at the fog top between -1.62 and -2.5 K h^{-1} (Maalick et al. 2016), -3.4 and -4.6 K h^{-1} (MB17), and -2.5 and -5.5 K h^{-1}

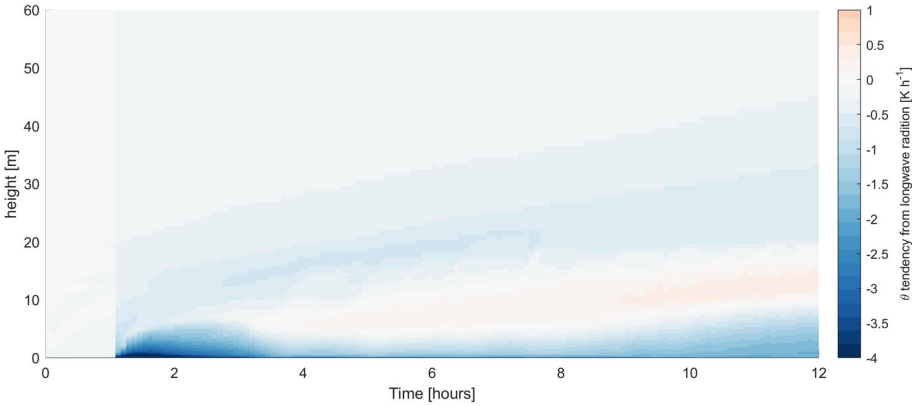

Fig. 5 Potential temperature tendency due to longwave radiative cooling

(Mazoyer et al. 2017). These are generally in line with the radiative cooling rates in our baseline simulation shown in Fig. 5, and we note that the higher radiative cooling rates found by both Mazoyer et al. (2017) and MB17 were for simulated fog with higher maximum liquid water mixing ratio than in case BASE.

Although nocturnal radiative cooling is an important process in the formation of continental radiation fog (see e.g., Maronga and Bosveld 2017; Price 2019), its relevance for the development of marine fog is still unclear. An investigation of marine fog off the west coast of the Korean Peninsula by Kim and Yum (2012b) found that longwave radiative cooling was a critical process in the formation of cold marine fog (i.e., air temperature greater than SST), regardless of the turbulence regime. Longwave cooling was also found to be an important factor in the maintenance of warm marine fog during a campaign off the west coast of the United States by Pilié et al. (1979). The presence or absence of shortwave radiative heating is not expected to play a significant role in the development of marine fog; climatology has revealed no significant diurnal trend in fog onset time at a coastal site in western South Korea (Kim and Yum 2010) or in the open ocean in the Grand Banks region of the North Atlantic (Isaac et al. 2020). Additionally, both Kim and Yum (2010) and Isaac et al. (2020) indicate that marine fog can often persist for several days at a time, with a median cold marine fog duration of 60 h found by Kim and Yum (2010). The simulations conducted herein all use a start time of 1200 UTC (0930 local time) and so the absence of shortwave heating is not significant in the fog formation; rather, diurnal shortwave heating acts to mitigate some of the temperature decrease caused by longwave radiative cooling.

As demonstrated here, the presence or absence of radiative cooling has a first-order effect on the fog development and maintenance: depending on the set-up, it can be a decisive factor in whether or not fog will form. Boutle et al. (2018) documented similar findings when the radiative effects of fog droplets were turned off in their sensitivity test, with no fog layer forming and visibility remaining high despite visibility dropping below 100 m in their control experiment where the radiative effects of fog droplets are considered.

Once fog has formed, radiative cooling at the fog top can interact with microphysical processes, strengthening and maintaining the fog development (this process is described in more detail in Sect. 3.3). This is similar to mechanisms at the top of stratocumulus clouds (de Lozar and Mellado 2015). Previous studies using LES have revealed that radiative cooling further affects the fog development through the following mechanism: radiative cooling at

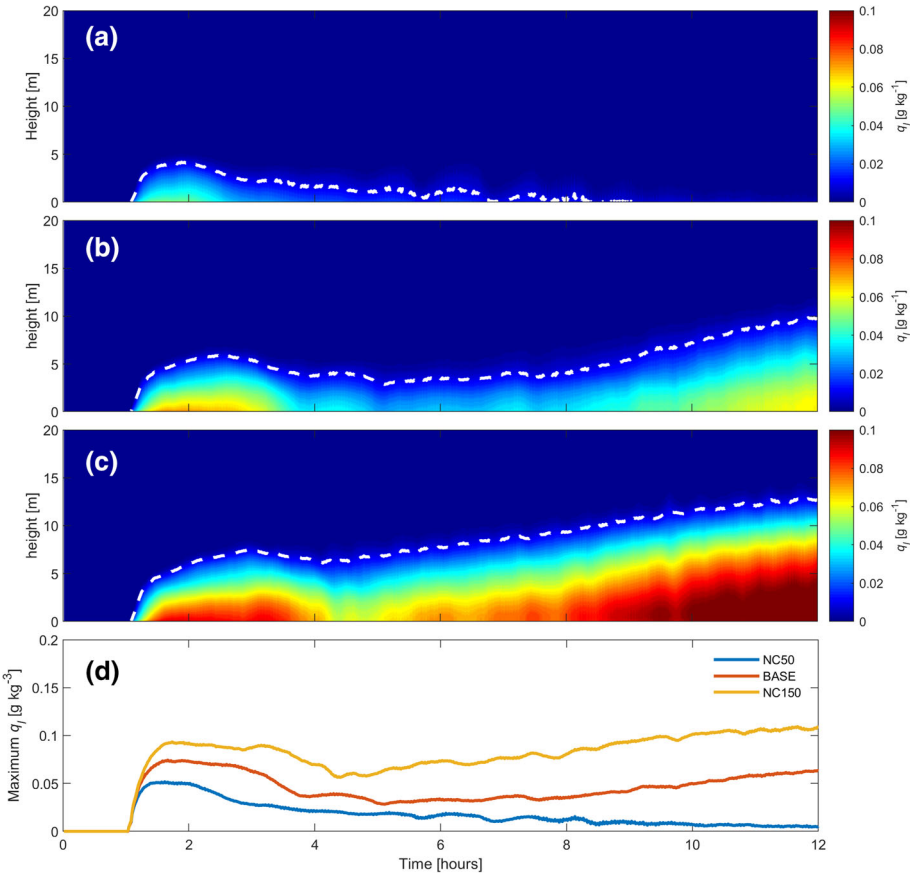

Fig. 6 Time–height plot of domain-averaged q_l for **a** case NC50 with $N_c = 50\,\mathrm{cm}^{-3}$, **b** case BASE with $N_c = 100\,\mathrm{cm}^{-3}$, **c** case NC150 with $N_c = 150\,\mathrm{cm}^{-3}$. Panel (d) shows the profile-maximum q_l (at any height) over the course of the 12-hour simulation

the fog top causes negative buoyancy, destabilizing the fog layer and resulting in top-down turbulent mixing within it (e.g., Kim and Yum 2012a; Mazoyer et al. 2017; Wærsted et al. 2019). This instability and resulting mixing is often further strengthened by heating from the surface, which may play a role in our simulations once the air temperature falls below the SST (see Sect. 3.4).

3.3 Sensitivity to Cloud Droplet Number Concentration

Figure 6 shows how the development of marine fog is influenced by N_c. When N_c is reduced from 100 (Fig. 6b) to 50 cm^{-3} (Fig. 6a), the fog strength in terms of q_l is considerably reduced during the development phase, and the fog begins to dissipate after 5 h. By 9 h, q_l has fallen below the threshold of 0.01 g kg^{-1} and the fog has fully dissipated. Conversely, when N_c is increased from 100 to 150 cm^{-3} a thicker fog develops (Fig. 6c), and the thickest part of the fog is also increased in depth compared to case BASE. All three cases show similar initial development of the fog; when the SST is lowered from 284 to 282 K at 1 h, fog

quickly develops. After a certain length of time, the fog begins to weaken and q_l decreases, which takes approximately 1 h in case NC50, 2 h in case BASE, and 2.5 h in case NC150. In case NC50 the fog never redevelops following this period of weakening, for case BASE it remains in the weaker state for several hours before growing in strength and depth, and in case NC150 the fog begins restrengthening within an hour and continues to grow throughout the simulation.

Case BASE has a maximum q_l of 0.07 g kg^{-1}; the corresponding values of cases NC50 and NC150 are 0.05 and 0.11 g kg^{-1}, respectively. After 12 h of simulation the maximum liquid water mixing ratio for case BASE is 0.06 g kg^{-1} at a height of within the lowest 1 m. For NC50 maximum liquid water mixing ratio at this time is 0.0054 g kg^{-1}, which is below the 0.01 g kg^{-1} threshold defined by MB17 and marked by the dashed white line in Fig. 6a. For NC150 the maximum q_l is 0.11 g kg^{-1} at a height of 1.1 m.

Figure 6 clearly illustrates that increasing N_c produces a denser fog with increased q_l, and slightly increases the depth of the fog. These findings are in agreement with MB17, who vary the fixed N_c value in idealized simulations of continental radiation fog based on measurements from the Cabauw tower in the Netherlands. In their simulations, increasing N_c from 150 to 200 cm^{-3} gives a 6% increase in maximum q_l, and decreasing from 150 to 100 cm^{-3} decreases q_l by 6%. In our simulations, at a time of 2 h, the maximum q_l is reduced by 33% when N_c is decreased from 100 to 50 cm^{-3} and increased by 26% when N_c is raised to 150 cm^{-3}. If the full time period from 1 to 12 h is considered, increasing N_c from 100 to 150 cm^{-3} increases the average maximum q_l by 89%, and reducing N_c to 50 cm^{-3} reduces the average maximum q_l by 40% (although this value will be biased by the dissipation of the fog in the later part of case NC50). As such, compared to MB17 our simulations show a much stronger response of q_l to the change in N_c, which may be partially due to the fact that moisture availability is not constrained by the land surface. Shipboard fog observations of LWC recorded during the C-FOG field campaign varied from 0.03 to 0.2 g cm^{-3} (see Fernando et al. 2020; Gultepe et al. 2020), indicating that the LWC values seen in our simulations are generally realistic for marine fog. Further details on the microphysical observations recorded during the C-FOG campaign can be found in Gultepe et al. (2020) and Wagh et al. (2020). A strong positive feedback between N_c and the depth of the fog layer is also noted by Schwenkel and Maronga (2019).

In single-moment microphysics schemes where N_c is held fixed, the effective radius (r_{eff}) of the droplets is adjusted in order to bring the saturation back down to 100% before the next model timestep. For a given supersaturation this results in smaller values of r_{eff} for a higher N_c as the equivalent amount of excess water must be spread over a larger number of droplets. Meanwhile, the optical depth of fog determines how much radiation can penetrate through the fog layer to the ground surface. Once fog becomes optically thick, radiative cooling from the fog top is enhanced, allowing the fog to grow deeper. Bergot (2013) identified this mechanism as a key feature of the fog life cycle in their LES study. The optical depth (τ) can be calculated as

$$\tau = \int_{z_1}^{z_2} \frac{3LWC}{2\rho_{\text{w}} r_{\text{eff}}} \mathrm{d}z, \tag{7}$$

where the variable LWC is the fog liquid water content, ρ_{w} is the density of liquid water, and z_1 and z_2 denote the heights of the top and bottom of the fog layer (Bendix 2002). When N_c is fixed, it is inversely proportional to r_{eff} and so for a given LWC this results in an optically thicker fog for higher values of N_c. As the fog grows optically thicker, increased radiative cooling at the fog-top layer cools the air immediately above the fog top to its saturation

temperature, creating a positive feedback and increasing the fog depth as well as hastening the transition to well-mixed fog, as described in Boutle et al. (2018).

A second mechanism where changing the fixed value of N_c can affect the fog is through gravitational settling. The rate of sedimentation of cloud droplets is directly related to droplet size. In the Morrison microphysics scheme the cloud-droplet fall velocity is parametrized as $V_c = 3 \times 10^7 D^2$, where D is droplet diameter. For higher N_c, the droplet size is reduced, lowering the droplet fall speed and increasing the length of time each droplet remains within the fog. During the initial fog development between 1 and 2 h, case NC50 shows maximum cloud-droplet fall speeds within the fog layer increased by 22% compared to case BASE over the same period. Over the same period case NC150 shows droplet fall-speed reductions of 4% compared to case BASE. For the same liquid water content, V_c will be inversely correlated with N_c via effects on the droplet effective radius. However, as the fog in case NC150 continues to strengthen over the simulation (Fig. 6c), by 12 h the liquid water content in case NC150 is sufficiently high that the cloud-droplet fall speed within the fog layer is comparable that in case BASE. This effect on sedimentation leads to droplets being removed from the fog at a more rapid rate in case NC50, which acts to reduce q_l as discussed in Schwenkel and Maronga (2019).

The strong effect that N_c has on q_l is of particular relevance for visibility. The visibility can be parametrized in the form

$$\text{Vis} = \frac{a}{(N_c LWC)^b}, \tag{8}$$

where a and b are constants that are empirically determined (e.g., Gultepe et al. 2017). The values of a and b have been determined for several coastal and marine fog events observed during the recent C-FOG campaign, and details can be found in Gultepe et al. (2020). Since altering N_c produces a positive feedback on LWC, the effect on the resulting visibility will be further compounded if it is parametrized in the form of Eq. 8. For the average values from our simulations, the term inside the brackets in the denominator is increased by a factor of 2.85 when N_c is changed from 100 to 150 cm^{-3}, and it is decreased by two thirds when N_c is reduced to 50 cm^{-3}. In this manner the stronger positive feedback of N_c on LWC seen in our study compared to that of MB17 will result in a considerably lower visibility for the same N_c when compared to their results. For example, if $b = 0.6473$ (as in Gultepe et al. 2006), then by increasing N_c from 100 to 150 cm^{-3} the visibility would be reduced by 50%; the same change in N_c reduces visibility by just 26% if applied to the results of MB17.

3.4 Sensitivity to Initial Air–Sea Temperature Difference

The effect of altering the SST on the domain-averaged q_l is shown in Fig. 7a, c, and e. At 2 h, the maximum q_l in case BASE is 0.07 g kg^{-1}, for case TDIFF1 it is 0.02 g kg^{-1}, and for case TDIFF4 it is 0.17 g kg^{-1}. However, in case BASE the fog decreases in strength after the initial formation (Fig. 3a), and the maximum q_l in TDIFF1 increases beyond that in BASE at 4 h. Although the maximum q_l is still increasing over the last few hours of the simulation in both BASE and TDIFF1, it remains high in TDIFF1 from 4 h onward. When the SST is lowered to 280 K (case TDIFF4), fog quickly forms, and continually increases in liquid water content throughout the course of the simulation. By 12 h, the maximum q_l for case BASE is 0.06 g kg^{-1} and this occurs within the lowest 1 m, for TDIFF1 it is 0.11 g kg^{-1} at a height of 1.3 m, and for TDIFF4 it is 0.29 g kg^{-1} at 23.6 m. The height of the fog top at this time is at 9.4 m in case BASE, 16.8 m in case TDIFF1, and 58.4 m in TDIFF4.

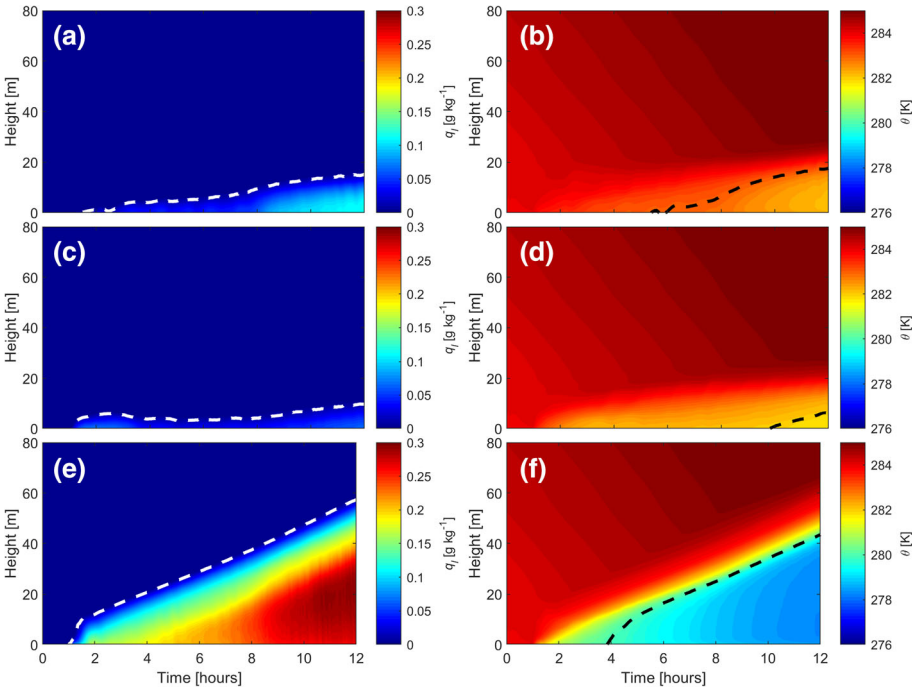

Fig. 7 Left: as in Figs. 3a, 6a–c but for **a** case TDIFF1 with $SST = 283$ K, **c** case BASE with $SST = 282$ K, **e** case TDIFF4 with $SST = 280$ K. The white dashed line shows the 0.01 g kg^{-1} threshold. Right: as in Fig. 3b but for (**b**) case TDIFF1, **d** case BASE, **f** case TDIFF4. The black dashed line shows the height where the air temperature is equal to the SST. Note that the colour scale for q_c differs from that used in Fig. 3

Lowering the fixed SST results in a much thicker fog, which is mainly caused by the much faster reduction in the potential temperature in case TDIFF4 (Fig. 7f). The minimum θ for case BASE at 3 h is 282.3 K, while for cases TDIFF1 and TDIFF4 the corresponding values are 283.3 K and 280.3 K, respectively, i.e., for each case the minimum θ at 3 h is 0.3 K higher than the corresponding SST.

By 6 h, the minimum θ values for the three cases are 282.2 K, 283.0 K, and 279.8 K; at 12 h these are 281.8 K, 282.1 K, and 278.2 K. From the black dashed line in Fig. 7b, d, f it can be seen that by 12 h the near-surface air temperature has fallen below the SST in each simulation. The near-surface air temperature decreases fastest in case TDIFF4 and slowest in TDIFF1; it decreases faster in BASE than TDIFF1, but the threshold of falling below the SST is reached faster in TDIFF1 due to the higher SST. For case BASE, the fog layer remains statically stable throughout the simulation, although the near-surface $\mathrm{d}\theta/\mathrm{d}z$ is close to zero by 12 h. However, in both cases TDIFF1 and TDIFF4, although the top portion of the fog layer and the area just above the fog layer remain statically stable throughout, $\mathrm{d}\theta/\mathrm{d}z$ becomes negative in the lowest part of the fog after 8 h in case TDIFF1 and 4 h in case TDIFF4, as the near-surface air temperature falls below the SST and continues to decrease further.

Figure 8 shows the time evolution of the domain-averaged surface θ flux and surface water vapour flux. The surface water vapour flux is calculated as

$$qv_{\mathrm{flux}} = C_q U_{10}(q_{vs,\mathrm{SST}} - q_{v,1})m_{\mathrm{a}}, \tag{9}$$

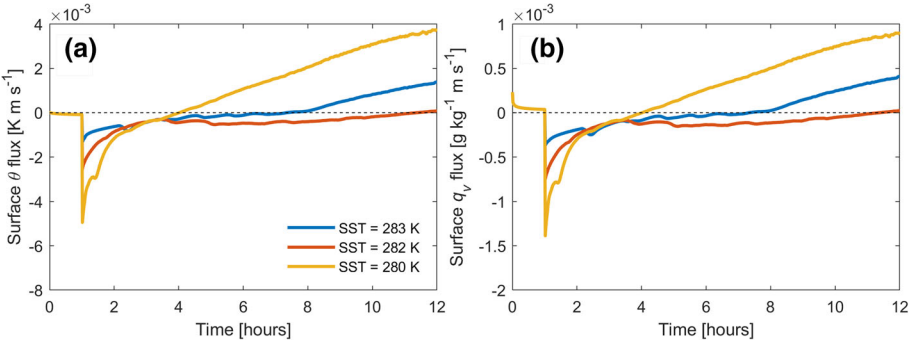

Fig. 8 **a** Surface θ flux for cases BASE, TDIFF1, and TDIFF4; **b** as (**a**) but for surface water vapour flux

where C_q is the surface exchange coefficient for moisture, U_{10} is the equivalent 10-m wind speed (based on the wind at the lowest model level), $q_{vs,SST}$ is the saturation vapour mixing ratio at the ocean surface calculated using the SST, $q_{v,1}$ is the water vapour mixing ratio at the lowest model level above the surface, and m_a is fractional moisture availability, which is equal to 1 here due to the ocean surface. As noted above, in the model the surface exchange coefficient is set to a constant of $C_q = 1.2 \times 10^{-3}$ following Drennan et al. (2007). Likewise, the surface θ flux is calculated as

$$\theta_{\text{flux}} = C_h U_{10}(\theta_{SST} - \theta_1), \tag{10}$$

where C_h is the surface exchange coefficient for sensible heat, also set as 1.2×10^{-3} following Drennan et al. (2007), θ_{SST} is the potential temperature of the sea surface, and θ_1 is the potential temperature at the lowest model level.

Figure 8a shows that the surface θ flux immediately becomes negative in each simulation when the SST is dropped at 1 h, as expected. The maximum negative surface θ flux is strongest for the highest air–sea temperature difference of 4 K (case TDIFF4). The strong negative surface θ and q_v fluxes in TDIFF4 quickly cool the near-surface air (Fig. 7f), and its temperature drops below the SST 4 h into the simulation, when the surface fluxes become positive. For case TDIFF1, the surface fluxes increase above zero after 8 h, and continue to increase with time; for case BASE the surface fluxes only become positive after 11.3 h, shortly before the end of the simulation.

Although the strongest fog is seen in the simulation with the highest air–sea temperature difference, the fog strength does not increase monotonically with ΔT. This reflects competing mechanisms driving the initial fog formation and maintenance: initially (at 1 h) the air–sea temperature difference drives the surface θ flux (i.e., a higher ΔT produces a stronger surface θ flux), allowing the air to more rapidly cool to saturation. However, although a higher ΔT gives a stronger surface heat flux and faster initial cooling, for higher ΔT the surface temperature has further to fall before reaching the SST. Once fog has formed, as the LWC increases, the fog may become optically thick and transition to well-mixed (see Sect. 3.3). This transition is aided by longwave cooling at the fog top, but upward heat flux from the sea surface can also contribute to the development of a well-mixed fog layer. After the fog becomes optically thick, a positive feedback between condensation and radiative cooling facilitates further vertical growth and strengthening of the fog (as discussed in Boutle et al. 2018; Schwenkel and Maronga 2019).

As outlined by Kim and Yum (2012a), when the sea surface is colder than the overlying air, the water vapour flux can be downward. Several other studies of fog in marine and coastal environments have also reported similar downward moisture fluxes (e.g., Edson et al. 2007; Heo et al. 2010; Grachev et al. 2020). If the overlying air is saturated or close to saturation and is warmer than the ocean surface, then it holds more water vapour than the air in contact with the sea surface, which is assumed to be at 100% saturation. Examining the vertical flux of water vapour for cases BASE, TDIFF1, and TDIFF4 reveals a positive water vapour flux within the lower portion of the developed fog in each case (not shown), and a negative water vapour flux just below the fog top. Since the SST remains constant after 1 h into each simulation, the height where the water vapour flux changes sign marks the level where the dewpoint temperature is equal to the SST. As the air within the fog layer is saturated, this height approximately corresponds to the dashed lines in Fig. 7b, d, and f.

Strong correlations between the air–sea temperature difference and the frequency of marine-fog formation have been noted in several previous studies. Cho et al. (2002) find that the highest frequency of occurrence of sea fog around the Korean Peninsula is in July and coincident with the largest average positive air–sea temperature difference; the same result was found for the Grand Banks region of the North Atlantic by Isaac et al. (2020). The Grand Banks region has one of the highest occurrences of marine fog in the world (a motivating factor for the C-FOG campaign), which is thought to be related to the shallow bathymetry of the Grand Banks combined with the southern edge of the cold Labrador Current (Dorman et al. 2017).

Additional simulations performed using a simplified initial profile (not shown) revealed that if ΔT is sufficiently high, the resulting strong negative surface heat flux can cool the near-surface air to saturation, even for initial relative humidities of 95% or lower. This demonstrates that for air masses that have high relative humidity but are not quite saturated (i.e., air masses that could be considered marginal for fog formation), cooling induced by a sudden strong reduction in the SST, such as passage over a cold current or a region of upwelling, could indeed induce sufficient low-level cooling to produce advection fog. The strong impact of SST on fog formation in a regional model is also noted in Edson et al. (2007), who highlight that high variability in SST is frequent in coastal areas, which creates additional challenges for fog forecasting in coastal regions.

Spatial and temporal variations in SST modify the sensible and latent heat fluxes, which affects the evolution of the fog (Heo and Ha 2010). Significant negative latent heat fluxes were recorded by Heo et al. (2010) during marine advection fog at the Ieodo Ocean Research Station in the Yellow Sea, and similar negative latent heat fluxes were found in coastal advection fog in Newfoundland during the C-FOG project by Grachev et al. (2020). It has been shown that coupled atmosphere–ocean regional-scale models are better able to reproduce the observed characteristics and spatial extent of sea fog than uncoupled or fixed-SST models (e.g., Heo and Ha 2010; Fallmann et al. 2019). Such regional-scale models highlight the effects of large-scale advection, which is represented in the current small-scale LES by advecting the domain across a sharp gradient of SST.

3.5 Sensitivity to Turbulent Mixing

The level of turbulent mixing during the fog is altered by changing the geostrophic wind speed from the baseline value of 3 m s^{-1} (see Table 1). A simulation with decreased forcing ($U_g = 2$ m s^{-1}; case U2) and one with higher forcing ($U_g = 4$ m s^{-1}; case U4) are performed. The response of the planar-averaged resolved TKE to geostrophic wind speed is shown in

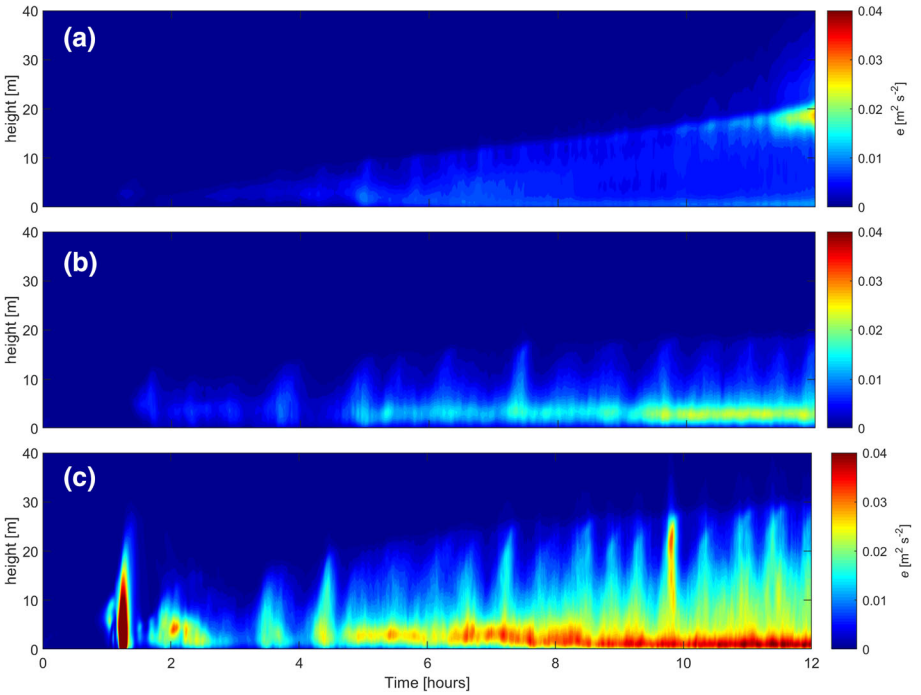

Fig. 9 Time–height plot of planar-averaged resolved e in $m^2\ s^{-2}$ for **a** case U2; **b** case BASE with $U_g = 3\ m\ s^{-1}$; **c** case U4

Fig. 9. The overall TKE is increased at higher wind speeds, as expected, due to increased generation of turbulent mixing. Cases BASE and U4 also show alternating phases of lower and higher TKE at the height of the fog top with a period of approximately 20–30 min. The average vertically-integrated resolved TKE during the last 6 h of the simulation is 0.40 $m^2\ s^{-2}$ for case BASE. For case U2 this is reduced by 25% to 0.30 $m^2\ s^{-2}$. When the geostrophic wind speed is increased to 4 m s^{-1}, the vertically-integrated TKE rises to 1.03 $m^2\ s^{-2}$, primarily driven by strong mixing within the lower portion fog layer once the fog is fully developed.

The domain-averaged q_l for each of the four turbulent mixing cases is shown in Fig. 10, with the white dashed line indicating the fog top for each case. Compared to case BASE, cases U2 and U4 both exhibit an increase in q_l. Following the initial fog formation, at times between 1 and 3 h, case U4 has the highest q_l, driven by strong mixing close to the surface. Both cases BASE and U4 show the fog decreasing in height and strength for a period of time after 3 h. However, in case U2 the fog continually strengthens throughout the simulation. The maximum q_l at 12 h is 0.06 g kg^{-1} in case BASE, 0.17 g kg^{-1} in case U2, and 0.15 g kg^{-1} in case U4.

The weaker the turbulent mixing, the more θ is able to decrease, and the minimum planar-averaged θ is consistently lowest for case U2 throughout the simulation (not shown). In case U4, the minimum θ remains higher since there is more vigorous mixing within the fog layer (Fig. 9c). In particular, strong bursts of mixing within the fog layer (such as that seen shortly before 10 h in Fig. 9c) enhance mixing with slightly warmer air from above, briefly increasing the potential temperature and temporarily depressing q_l throughout the fog layer (Fig. 10c).

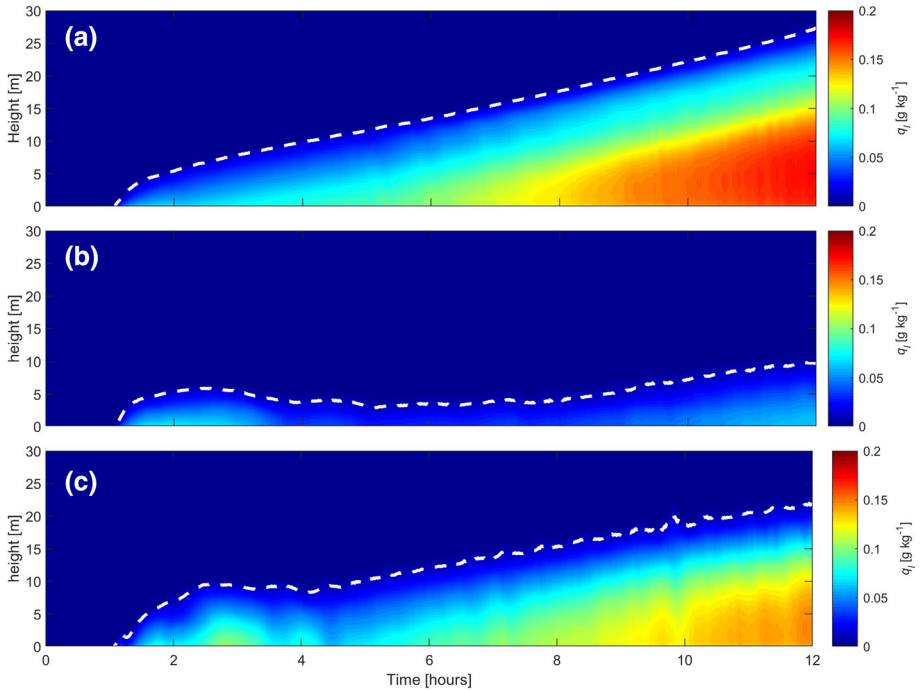

Fig. 10 Time–height plot of planar-averaged q_c in g kg^{-1} for **a** case U2; **b** case BASE with $U_g = 3$ m s^{-1}; **c** case U4. The white dashed line represents a threshold of $q_c = 0.01$ g kg^{-1}. Note that the colour scale differs from that used for q_c in Fig. 6

The height of the fog top is also compared among the three cases, as depicted by the white dashed line in Fig. 10. The initial vertical fog growth is fastest in U4, but the vertical growth stalls and the fog decreases in strength from 3 h onward, before again beginning to grow and strengthen at 4.5 h, similar to case BASE (see Sect. 3.1). In case U2, the height of the fog top continues to grow at a steady rate throughout the simulation. MB17 and Guedalia and Bergot (1994) both report an increase in the height of the fog top under scenarios with higher turbulent mixing. The results presented herein do not show this monotonic relationship, although additional simulations conducted with a simplified initial profile in which θ increased linearly with height and q_v linearly decreased showed faster growth of the fog top under higher geostrophic wind speeds. The non-monotonicity seen in the present simulations reflects the role of turbulent mixing, and it would be anticipated that at still higher values of U_g the fog would fail to develop due to warm, dry air transported downwards.

Figure 11 shows an $x - z$ slice at $y = 128$ m (the centre of the domain) after 11 h of simulation for each of the turbulent mixing cases. Although the fog in each case covers the full lateral extent of the domain, q_c is not homogeneous across the domain and individual plumes with higher q_c are clearly visible. When the full planar average is considered, q_c generally decreases with height, but at individual locations the highest q_c may not necessarily be close to the surface (e.g., around $x = 180$ m in Fig. 11a, and at $x = 220$ m in Fig. 11c).

Previous sensitivity analyses of the timing of key fog-life-cycle markers to turbulent mixing by MB17 surprisingly find that the timing of fog onset is delayed compared to their baseline case (which had a wind speed of 4 m s^{-1}) when the turbulent mixing was either

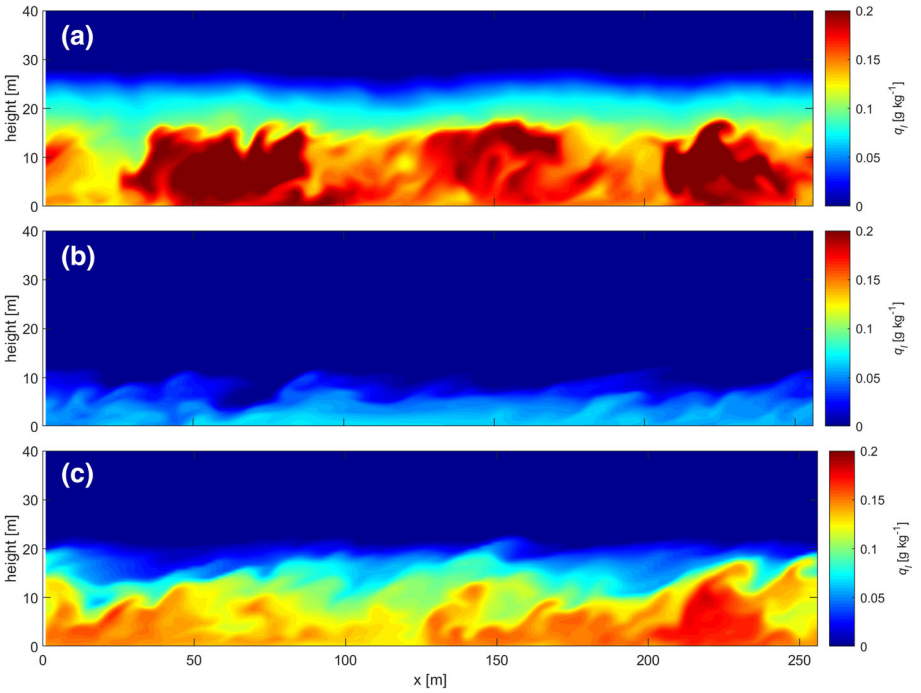

Fig. 11 $x - z$ slice of q_l in g kg^{-1} at 11 h into the simulation for **a** case U2; **b** case BASE with $U_g = 3$ m s^{-1}; **c** case U4

increased or decreased. The delayed fog onset for stronger turbulent mixing was ascribed to the effect of strong upward mixing of cold surface air and corresponding downward mixing of warmer air above. Since the initial fog formation in our simulations is driven by the increase in air–sea temperature difference, unlike MB17 we do not see an impact of turbulent mixing on the timing of fog formation. However there is clearly an impact on the development and maintenance of the fog in terms of strength and depth (see Figs. 10 and 11); in the simulations presented herein, a non-linear response of the fog strength (in terms of liquid water content) to increasing turbulent mixing is found.

Although Fig. 10 shows that the maximum q_l increases as the wind speed either increases from 3 to 4 m s^{-1} or decreases from 3 to 2 m s^{-1}, additional simulations performed using different initial conditions (not shown), with linearly decreasing relative humidity with height, did not show this result. Rather, with a different initial profile, the strongest fog was seen at an intermediate wind speed of 3 m s^{-1}, and at higher wind speeds strong mixing at the fog top caused entrainment of drier air from above, causing the fog to dissipate more quickly at higher wind speeds. This further underlines results from previous studies which have shown that the role of turbulent mixing in fog is complex, and can facilitate or impede fog development, strengthening, and dissipation, depending on the set-up (as in MB17). If there exists a sufficiently deep layer that is close to saturation, then increased mixing can cause rapid growth of fog throughout that layer. If, on the other hand, a strong capping inversion is present at a relatively low height, then entrainment of warm and dry air into the fog layer from above can result in erosion of the fog from the top downward.

Previous studies of continental radiation fog, both numerical and experimental, have suggested a maximum wind speed above which fog cannot be maintained; for radiation fog this is widely accepted. However, coastal and marine fog driven primarily by advection has been recorded at wind speeds of 10 m s^{-1} or higher (e.g., Filonczuk et al. 1995; Isaac et al. 2020), and so further work is necessary to improve our understanding of the impact of turbulent mixing on fog at higher wind speeds in the marine environment.

4 Conclusions

In this study large-eddy simulation of an idealized marine fog event is used to study the sensitivity of the fog depth, thickness, and macrostructure to several physical and microphysical parameters. The sensitivity of the fog to radiative cooling, turbulent mixing, initial air–sea temperature difference, and prescribed cloud-droplet number concentration is tested, finding that fog formation and strength is highly sensitive to all four of these factors. This finding has important implications on the expected ability of NWP models to accurately represent marine fog formation and dissipation. In particular, longwave radiative cooling is found to be a key process in the fog formation, in line with previous work by Pilié et al. (1979) and Kim and Yum (2012b); depending upon the surface-layer relative humidity in the initial profile, radiative cooling can be a critical factor in whether or not saturation is reached. After fog formation, longwave radiative cooling then plays an important role in fog development and maintenance via interactions with microphysical processes as described in Sect. 3.3.

In this study, a commonly used single-moment microphysics scheme is evaluated (Morrison et al. 2005), where the cloud-droplet number concentration is prescribed. Altering this value is found to have significant impacts on the strength of the fog in terms of liquid water content and the resulting visibility. Altering the value of N_c from 100 to 150 cm^{-3} increases the maximum liquid water content by 89% over the whole simulation, whereas when the same change in N_c is made by MB17 the LWC only changes by 6%. The stronger effect in our simulations is likely due to the simplified surface scheme used in CM1, as well as the ocean surface providing a constant and unimpeded source of moisture. Changing N_c alters the droplet effective radius, directly impacting the longwave radiative cooling through effects on the optical depth as outlined previously by Maalick et al. (2016) and MB17; the change in effective radius additionally impacts microphysical processes via gravitational settling (Schwenkel and Maronga 2019). As described in Sect. 3.3, the positive feedback between N_c and LWC has a strong effect on the visibility and could potentially result in reduced visibility for marine fog compared to continental fog for the same N_c due to the difference in the impact on LWC that unlimited surface moisture allows. This nonlinear response of fog properties to N_c again has implications in NWP efforts, especially when single-moment microphysical schemes with default values of N_c are used.

The sensitivity to the initial air–sea temperature difference is tested by adjusting the fixed SST value. The results in Sect. 3.4 indicate that relatively small changes in the SST have a large impact on the resulting fog. The strongest fog in any of the simulations performed occurred when the air–sea temperature difference was highest. Further tests (not shown) indicated that a sufficiently high air–sea temperature difference can cause strong enough cooling for air masses to reach saturation that would otherwise remain subsaturated over higher SST. This corresponds with observations from Cho et al. (2002) and Isaac et al. (2020) that fog frequency in regions prone to marine fog is maximized when the air–sea temperature difference is greatest. In this study, it is assumed that SST remains unchanged on time scales

of the order of several hours. Given the importance of SST on the fog development, however, it would be of interest for future studies to include the effect of a time-varying SST, so that the impact of spatial or temporal variation in SST could be better examined.

The role of turbulent mixing in fog is complex and has served as a focal point in several previous investigations due to the competition between excessive mixing and entrainment of upper-level warm or dry air and the role of turbulence in deepening an incipient fog layer (MB17; Price et al. 2018). In this study the impact of turbulent mixing is examined by conducting a suite of simulations with varying geostrophic wind speeds. A non-monotonic relationship is found between turbulent mixing and the strength of the resulting fog. Additional sensitivity tests that were conducted with different initial profiles showed contrasting results (not shown), with the strongest fog occurring at a geostrophic wind speed of $3\,\mathrm{m\,s^{-1}}$, and both increases and decreases in wind speed reducing the fog strength. This further highlights the difficulty of untangling the role of turbulent mixing on fog development, and further supports the comments of MB17 that the effect of turbulent mixing on fog depends heavily on the set-up. Unlike continental radiation fog, advection fog in a coastal or marine environment can occur at relatively high wind speeds (e.g., Chen et al. 2019), and therefore LES provides a powerful way of investigating the mechanisms which lead to this discrepancy.

The results presented in this study demonstrate that accurate prediction of fog properties will be achieved only with a better understanding and representation of the small-scale physical mechanisms that control the system. In marine fog specifically, measurements are relatively scarce and observational campaigns are logistically challenging, and therefore LES serves as a platform for constraining parametrizations used at coarser scales. Despite considerable improvement in NWP models, accurate forecasting of fog remains a challenge (van der Velde et al. 2010) due to the nature of fog as a 'threshold phenomenon' (Bergot and Guedalia 1994) and the considerable computational expense required to simulate the stable boundary layer at high resolution (e.g., MB17). Here it is demonstrated that simulations of marine fog are highly sensitive to the handling of several physical and microphysical processes, as illustrated for continental radiation fog using a one-dimensional model by Bergot and Guedalia (1994) and more recently using LES by MB17.

The inability to compare directly with measurements is a limitation of our study, and remains a significant challenge in marine fog modelling. Despite the importance of marine fog as a transportation hazard, and the related economic impact, observations of fog over the open ocean remain relatively scarce. This underscores the importance of targeted field campaigns such as C-FOG (Fernando et al. 2020), and highlights the need for continued efforts and innovation in collecting observations in marine fog events, while cognisant of the inherent logistical difficulties.

Acknowledgements This research was funded by the Office of Naval Research Award N00014-18-1-2472 entitled Toward Improving Coastal Fog Prediction (C-FOG). Computer resources were made available through the Notre Dame Center for Research Computing and the DoD High Performance Computing Modernization Program.

References

Abdul-Razzak H, Ghan J (2000) A parameterization of aerosol activation 2. Multiple aerosol types. J Geophys Res 105:6837–6844

Beare RJ, Macvean MK, Holtslag AAM, Cuxart J, Esau I, Golaz JC, Jimenez MA, Khairoutdinov M, Kosovic B, Lewellen D, Lund TS, Lundquist JK, McCabe A, Moene AF, Noh Y, Raasch S, Sullivan P (2006)

An intercomparison of large-eddy simulations of the stable boundary layer. Boundary-Layer Meteorol 118(2):247–272. https://doi.org/10.1007/s10546-004-2820-6
Bendix J (2002) A satellite-based climatology of fog and low-level stratus in Germany and adjacent areas. Atmos Res 64(1–4):3–18. https://doi.org/10.1016/S0169-8095(02)00075-3
Bergot T (2013) Small-scale structure of radiation fog: a large-eddy simulation study. Q J R Meteorol Soc 139(673):1099–1112. https://doi.org/10.1002/qj.2051
Bergot T (2016) Large-eddy simulation study of the dissipation of radiation fog. Q J R Meteorol Soc 142(695):1029–1040
Bergot T, Guedalia D (1994) Numerical forecasting of radiation fog. Part I: numerical model and sensitivity tests. Mon Weather Rev 122(6):1218–1230
Boutle I, Price J, Kudzotsa I, Kokkola H, Romakkaniemi S (2018) Aerosol-fog interaction and the transition to well-mixed radiation fog. Atmos Chem Phys 18(11):7827–7840
Brown R, Roach WT (1976) The physics of radiation fog: II a numerical study. Q J R Meteorol Soc 102(432):335–354
Bryan GH, Morrison H (2011) Sensitivity of a simulated squall line to horizontal resolution and parameterization of microphysics. Mon Weather Rev 140(1):202–225. https://doi.org/10.1175/mwr-d-11-00046.1
Chen J, Han B, Yang Q, Wei L, Zeng Y, Wu R, Zhang L, Ding Z (2019) Analysis of a sea fog episode at King George Island, Antarctica. Atmosphere 10(10):585
Cho YK, Kim MO, Kim BC (2002) Sea fog around the Korean Peninsula. J Appl Meteorol 39(12):2473–2479
de Lozar A, Mellado JP (2015) Mixing driven by radiative and evaporative cooling at the stratocumulus top. J Atmos Sci 72:4681–4700. https://doi.org/10.1175/JAS-D-15-0087.1
Deardorff JW (1980) Stratocumulus-capped mixed layers derived from a three-dimensional model. Boundary-Layer Meteorol 18:495–527
Donelan MA, Haus BK, Reul N, Plant WJ, Stiassnie M, Graber HC, Brown OB, Saltzman ES (2004) On the limiting aerodynamic roughness of the ocean in very strong winds. Geophys Res Lett 31(18)
Dorman C, Mejia J, Koracin D, McEvoy D (2017) Worldwide marine fog occurrence and climatology. In: Koračin D, Dorman C (eds) Marine Fog: challenges and advancements in observations, modeling, and forecasting. Springer, Cham, pp 7–152
Dorman CE, Koračin D (2017) Marine fog: challenges and advancements in observations, modeling and forecasting. Springer, Cham, p 537
Drennan WM, Zhang JA, French JR, McCormick C, Black PG (2007) Turbulent fluxes in the hurricane boundary layer. Part II: latent heat flux. J Atmos Sci 64(4):1103–1115
Duynkerke PG (1991) Radiation fog: a comparison of model simulation with detailed observations. Mon Weather Rev 119:324–341
Duynkerke PG (1999) Turbulence, radiation and fog in Dutch stable boundary layers. Boundary-Layer Meteorol 90(3):447–477. https://doi.org/10.1023/A:1026441904734
Edson J, Crawford T, Crescenti J, Farrar T, Frew N, Gerbi G, Helmis C, Hristov T, Khelif D, Jessup A, Jonsson H, Li M, Mahrt L, McGillis W, Plueddemann A, Shen L, Skyllingstad E, Stanton T, Sullivan P, Sun J, Trowbridge J, Vickers D, Wang S, Wang Q, Weller R, Wilkin J, Williams AJ, Yue DK, Zappa C (2007) The coupled boundary layers and air-sea transfer experiment in low winds. Bull Am Meteorol Soc 3:341–356. https://doi.org/10.1175/BAMS-88-3-341
Edwards JM (2009) Radiative processes in the stable boundary layer: Part I. Radiative aspects. Boundary-Layer Meteorol 131(2):105–126. https://doi.org/10.1007/s10546-009-9364-8
Fairall CW, Bradley EF, Hare JE, Grachev AA, Edson JB (2003) Bulk parameterization of air-sea fluxes: updates and verification for the COARE algorithm. J Clim 16(4):571–591
Fallmann J, Lewis H, Sanchez JC, Lock A (2019) Impact of high-resolution ocean-atmosphere coupling on fog formation over the North Sea. Q J R Meteorol Soc 145(720):1180–1201. https://doi.org/10.1002/qj.3488
Fernando HJS, Gultepe I, Dorman C, Pardyjak E, Wang Q, Hoch SW, Richter D, Creegan E, Gaberšek S, Bullock T, Hocut C, Chang R, Alappattu D, Dimitrova R, Flagg D, Grachev A, Krishnamurthy R, Singh DK, Lozovatsky I, Nagare B, Sharma A, Wagh S, Wainwright C, Wroblewski M, Yamaguchi R, Bardoel S, Coppersmith RS, Chisholm N, Gonzalez E, Gunawardena N, Hyde O, Morrison T, Olson A, Perelet A, Perrie W, Wang S, Wauer B (2020) C-FOG: life of coastal fog. Bull Am Meteorol Soc. https://doi.org/10.1175/BAMS-D-19-0070.1 (in press)
Filonczuk MK, Cayan DR, Riddle LG (1995) Variability of marine fog along the California Coast. Tech Rep, Climate Research Division, Scripps Institution of Oceanography, San Diego, California, USA, p 93
Grachev AA, Krishnamurthy R, Fernando HJS, Fairall CW, Bardoel SL, Wang S (2020) Atmospheric turbulence measurements in coastal zone with and without fog. Submitted to Boundary-Layer Meteorol

Guedalia D, Bergot T (1994) Numerical forecasting of radiation fog. Part II: a comparison of model simulation with several observed fog events. Mon Weather Rev 6(122):1231–1246

Gultepe I, Müller MD, Boybeyi Z (2006) A new visibility parameterization for warm-fog applications in numerical weather prediction models. J Appl Meteorol Climatol 45(11):1469–1480. https://doi.org/10.1175/JAM2423.1

Gultepe I, Tardif R, Michaelides SC, Cermak J, Bott A, Bendix J, Müller MD, Pagowski M, Hansen B, Ellrod G, Jacobs W, Toth G, Cober SG (2007) Fog research: a review of past achievements and future perspectives. Pure Appl Geophys 164(6–7):1121–1159. https://doi.org/10.1007/s00024-007-0211-x

Gultepe I, Pearson G, Milbrandt JA, Hansen B, Platnick S, Taylor P, Gordon M, Oakley JP, Cober SG (2009) The fog remote sensing and modeling field project. Bull Am Meteorol Soc 90(6–7):341–360

Gultepe I, Milbrandt J, Zhao B (2017) Marine Fog: a review on microphysics and visibility prediction. In: Koračin D, Dorman C (eds) Marine Fog: challenges and advancements in observations, modeling, and forecasting. Springer, Cham, pp 345–394

Gultepe I, Fernando HJS, Pardyjak E, Dorman CE, J HA, Wang Q, Creegan E, Hoch SW, Flagg DD, Yamaguchi R, Krishnamurthy R, Gaberšek S, Perrie W, Perelet A, Singh DK, Chang R, Nagare B, Wagh S, Wang S (2020) A review of coastal fog microphysics during C-FOG. Submitted to Boundary-Layer Meteorol

Haeffelin M, Bergot T, Elias T, Tardif R, Carrer D, Chazette P, Colomb M, Drobinski P, Dupont E, Dupont JC, Gomes L, Musson-Genon L, Pietras C, Plana-Fattori A, Protat A, Rangognio J, Raut JC, Rémy S, Richard D, Sciare J, Zhang X (2010) PARISFOG: shedding new light on fog physical processes. Bull Am Meteorol Soc 91(6):767–783. https://doi.org/10.1175/2009BAMS2671.1

Hammer E, Gysel M, Roberts GC, Elias T, Hofer J, Hoyle CR, Bukowiecki N, Dupont JC, Burnet F, Baltensperger U, Weingartner E (2014) Size-dependent particle activation properties in fog during the ParisFog 2012/13 field campaign. Atmos Chem Phys 14(19):10,517–10,533. https://doi.org/10.5194/acp-14-10517-2014

Heo KY, Ha KJ (2010) A coupled model study on the formation and dissipation of sea fogs. Mon Weather Rev 138(4):1186–1205. https://doi.org/10.1175/2009mwr3100.1

Heo KY, Ha KJ, Mahrt L, Shim JS (2010) Comparison of advection and steam fogs: from direct observation over the sea. Atmos Res 98:426–437. https://doi.org/10.1016/j.atmosres.2010.08.004

Hudson JG (1980) Relationship between fog condensation nuclei and fog microstructure. J Atmos Sci 37(8):1854–1867. https://doi.org/10.1175/1520-0469(1980)037<1854:rbfcna>2.0.co;2

Iacono MJ, Delamere JS, Mlawer EJ, Shephard MW, Clough SA, Collins WD (2008) Radiative forcing by long-lived greenhouse gases: calculations with the AER radiative transfer models. J Geophys Res Atmos 113(13):2–9. https://doi.org/10.1029/2008JD009944

Isaac G, Bullock T, Beale J, Beale S (2020) Characterizing and predicting marine fog offshore Newfoundland and Labrador. X-X, Weather Forecast X(X). https://doi.org/10.1175/WAF-D-19-0085.1

Kim CK, Yum SS (2010) Local meteorological and synoptic characteristics of fogs formed over Incheon international airport in the west coast of Korea. Adv Atmos Sci 27(4):761–776. https://doi.org/10.1007/s00376-009-9090-7

Kim CK, Yum SS (2012a) A numerical study of sea-fog formation over cold sea surface using a one-dimensional turbulence model coupled with the Weather Research and Forecasting model. Boundary-Layer Meteorol 143(3):481–505. https://doi.org/10.1007/s10546-012-9706-9

Kim CK, Yum SS (2012b) Marine boundary layer structure for the sea fog formation off the west coast of the Korean Peninsula. Pure Appl Geophys 169(5–6):1121–1135. https://doi.org/10.1007/s00024-011-0325-z

Koračin D, Dorman CE, Lewis JM, Hudson JG, Wilcox EM, Torregrosa A (2014) Marine fog: a review. Atmos Res 143:142–175. https://doi.org/10.1016/j.atmosres.2013.12.012

Li Y, Zheng Y (2015) Analysis of atmospheric turbulence in the upper layers of sea fog. Chin J Oceanol Limnol 33(3):809–818. https://doi.org/10.1007/s00343-015-4030-0

Maalick Z, Kühn T, Korhonen H, Kokkola H, Laaksonen A, Romakkaniemi S (2016) Effect of aerosol concentration and absorbing aerosol on the radiation fog life cycle. Atmos Environ 133:26–33

Maronga B, Bosveld F (2017) Key parameters for the life cycle of nocturnal radiation fog: a comprehensive large-eddy simulation study. Q J R Meteorol Soc 143(707):2463–2480

Mazoyer M, Lac C, Thouron O, Bergot T, Masson V, Musson-Genon L (2017) Large eddy simulation of radiation fog: impact of dynamics on the fog life cycle. Atmos Chem Phys 17(13):017

Morrison H, Curry JA, Khvorostyanov VI (2005) A new double-moment microphysics parameterization for application in cloud and climate models. Part I: description. J Atmos Sci 62(6):1665–1677. https://doi.org/10.1175/JAS3446.1

Nakanishi M (2000) Large-eddy simulation of radiation fog. Boundary-Layer Meteorol 94(3):461–493. https://doi.org/10.1023/A:1002490423389

Pilié RJ, Mack EJ, Rogers CW, Katz U, Kocmond WC (1979) The formation of marine fog and the development of fog-stratus systems along the California coast. J Appl Meteorol 18:1275–1286

Poku C, Ross AN, Blyth AM, Hill AA, Price JD (2019) How important are aerosol-fog interactions for the successful modelling of nocturnal radiation fog? Weather 74(7):237–243. https://doi.org/10.1002/wea.3503

Porson A, Price J, Lock A, Clark P (2011) Radiation fog. Part II: large-eddy simulations in very stable conditions. Boundary-Layer Meteorol 139(2):193–224. https://doi.org/10.1007/s10546-010-9579-8

Price J (2019) On the formation and development of radiation fog: an observational study. Boundary-Layer Meteorol 172:167–197

Price J, Lane S, Boutle I, Smith DKE, Bergot T, Lac C, Duconge L, McGregor J, Kerr-Munslow A, Pickering M, Clark R (2018) LANFEX: a field and modeling study to improve our understanding and forecasting of radiation fog. Bull Am Meteorol Soc 99(10):2061–2077

Schwenkel J, Maronga B (2019) Large-eddy simulation of radiation fog with comprehensive two-moment bulk microphysics: impact of different aerosol activation and condensation parameterizations. Atmos Chem Phys 19(10):7165–7181. https://doi.org/10.5194/acp-19-7165-2019

Smagorinsky J (1963) General circulation experiments with the primitive equations I. The basic experiment. Mon Weather Rev 91:99–164

Stolaki S, Haeffelin M, Lac C, Dupont JC, Elias T, Masson V (2015) Influence of aerosols on the life cycle of a radiation fog event. A numerical and observational study. Atmos Res 151:146–161

Tardif R (2007) The impact of vertical resolution in the explicit numerical forecasting of radiation fog: a case study. Pure Appl Geophys 164(6–7):1221–1240. https://doi.org/10.1007/s00024-007-0216-5

Thouron O, Brenguier JL, Burnet F (2012) Supersaturation calculation in large eddy simulation models for prediction of the droplet number concentration. Geosci Model Dev 5(3):761–772. https://doi.org/10.5194/gmd-5-761-2012

Twomey S (1959) The nuclei of natural cloud formation part II: the supersaturation in natural clouds and the variation of cloud droplet concentration. Pure Appl Geophys 43:243–249

van der Velde IR, Steeneveld GJ, Wichers Schreur BGJ, Holtslag AAM (2010) Modeling and forecasting the onset and duration of severe radiation fog under frost conditions. Mon Weather Rev 138(11):4237–4253. https://doi.org/10.1175/2010mwr3427.1

Wærsted EG, Haeffelin M, Steeneveld GJ, Dupont JC (2019) Understanding the dissipation of continental fog by analysing the LWP budget using idealized LES and in situ observations. Q J R Meteorol Soc 145:784–804. https://doi.org/10.1002/qj.3465

Wagh S, Krishnamurthy R, Wainwright C, Wang S, Dorman C, Fernando HJS, Gultepe I (2020) Microphysics of marine fog during stratus cloud base lowering. Submitted to Boundary-Layer Meteorol

Wang S, Fernando HJS, Creegan E, Krishnamurthy R, Wainwright C, Wagh S (2020) Analysis of a coastal marine fog episode during C-FOG. Submitted to Boundary-Layer Meteorol